

Supplementary Information

for

Thermal Stability and Electronic and Magnetic Properties of Atomically Thin 2D Transition Metal Oxides

Heleen van Gog,¹ Wun-Fan Li,¹ Changming Fang,² Rik S. Koster,¹
Marjolein Dijkstra,¹ Marijn A. van Huis¹

¹ Soft Condensed Matter, Debye Institute for Nanomaterials Science,
Utrecht University, Princetonplein 5, 3584 CC Utrecht, The Netherlands

² Institute of Materials and Manufacturing, Kingston Lane, Uxbridge,
Middlesex UB8 3PH, Brunel University London, United Kingdom

Corresponding authors: h.vangog@uu.nl; m.a.vanhuis@uu.nl

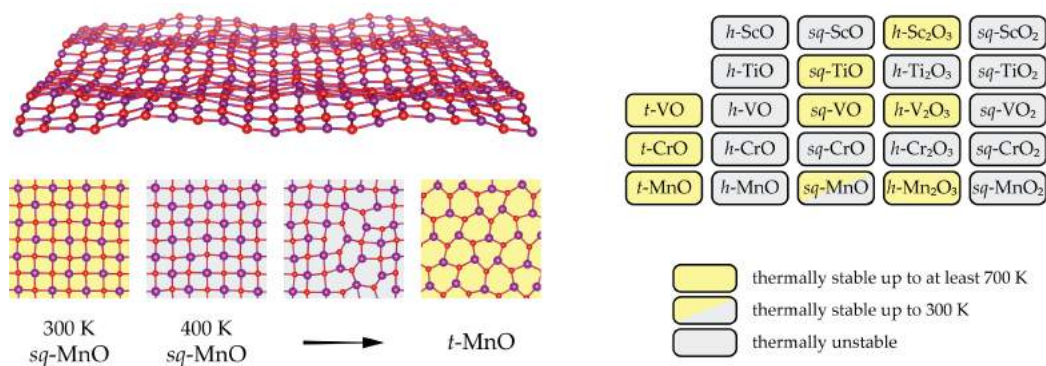


Table S1. The formation energy E_f (eV/atom), the buckling energy E_b (meV/atom), and the size of buckling d_b (Å) for all 2D TMOs. Bold dark-blue formation energies denote lowest-energy configurations. A negative (positive) E_b indicates that a buckled (planar) structure is energetically more stable than its planar (buckled) counterpart. Fields with — indicate that a buckled input configuration relaxed into a planar configuration, or that a specific magnetic input configuration relaxed into a non-magnetic (NM) configuration. For the t -MOs, “(a)” and “(b)” refer to the configurations shown in Figure 5a and 5b, respectively.

	NM			FM			AFM1			AFM2		
	E_f	E_b	d_b	E_f	E_b	d_b	E_f	E_b	d_b	E_f	E_b	d_b
t -VO (a)	-1.192	-10	0.49	-1.317	—	—	-1.332	-6	0.45	-1.335	-5	0.44
t -VO (b)	-1.140	-54	0.47	-1.269	—	—	-1.260	11	0.39	-1.243	14	0.42
t -CrO (a)	-0.744	61	0.57	-1.071	—	—	-1.158	—	—	-1.174	—	—
t -CrO (b)	-0.699	-130	0.53	-1.029	—	—	-1.051	-6	0.20	-1.038	-13	0.85
t -MnO (a)	-0.628	—	—	-1.016	—	—	-1.153	—	—	-1.127	—	—
t -MnO (b)	-0.565	—	—	-1.144	—	—	-1.208	—	—	-1.142	—	—
	NM			FM			AFM			FiM		
	E_f	E_b	d_b	E_f	E_b	d_b	E_f	E_b	d_b	E_f	E_b	d_b
h -ScO	-2.350	-14	0.35	-2.359	-23	0.53	-2.367	-31	0.52	-2.344	—	—
h -TiO	-1.753	-39	0.71	-1.742	—	—	-1.735	—	—	—	—	—
h -VO	-1.084	52	0.77	-1.261	-47	0.39	-1.212	—	—	-1.196	—	—
h -CrO	-0.567	112	0.62	-0.931	-2	0.24	-1.038	—	—	-1.001	0	0.11
h -MnO	-0.435	-78	0.39	-1.016	—	—	-1.137	—	—	-1.130	—	—
	NM			FM			AFM1			AFM2		
	E_f	E_b	d_b	E_f	E_b	d_b	E_f	E_b	d_b	E_f	E_b	d_b
sq -ScO	-2.470	—	—	—	—	—	—	—	—	—	—	—
sq -TiO	-1.884	—	—	-1.891	—	—	-1.942	—	—	-1.910	—	—
sq -VO	-1.200	-20	0.25	-1.331	—	—	-1.430	—	—	-1.380	11	0.21
sq -CrO	-0.660	-81	0.50	-1.103	—	—	-1.250	-7	0.22	-1.248	—	—
sq -MnO	-0.476	-90	0.55	-1.087	—	—	-1.098	—	—	-1.055	—	—
	NM			FM			AFM					
	E_f	E_b	d_b	E_f	E_b	d_b	E_f	E_b	d_b			
h -Sc ₂ O ₃	-2.713	—	—	—	—	—	—	—	—			
h -Ti ₂ O ₃	-2.239	-8	0.22	-2.307	-7	0.26	-2.315	-1	0.14			
h -V ₂ O ₃	-1.590	11	0.32	-1.821	—	—	-1.711	—	—			
h -Cr ₂ O ₃	-1.135	-6	0.21	-1.394	—	—	-1.359	—	—			
h -Mn ₂ O ₃	-0.956	—	—	-1.222	—	—	-1.225	(FiM)	—			
	NM			FM			AFM1			AFM1		
	E_f	E_b	d_b	E_f	E_b	d_b	E_f	E_b	d_b	E_f	E_b	d_b
sq -ScO ₂	-1.935	—	—	-1.980	—	—	—	—	—	-1.948	(FiM)	—
sq -TiO ₂	-2.144	—	—	—	—	—	—	—	—	—	—	—
sq -VO ₂	-1.600	5	0.13	-1.681	2	0.15	-1.680	-1	0.10	-1.678	-1	0.11
sq -CrO ₂	-1.173	—	—	-1.378	—	—	-1.338	—	—	-1.362	—	—
sq -MnO ₂	-0.925	—	—	-1.036	—	—	-1.114	—	—	-1.091	—	—

Table S2. Properties (space group, magnetic ordering, and conductivity) of the bulk TMO phases chosen in this study as the 2D TMOs' corresponding 3D phases; and coordination numbers (CNs) and TM–O bond lengths ($d_{\text{TM-O}}$) for these 2D and 3D TMOs. Bond lengths are averaged values; real bond length difference for 3D TMOs is within 9%. Structural parameters and magnetic orderings that were not found in literature were calculated in this study; with the exception of ScO_2 , which was omitted. SC: semiconductor, SM: semimetal, HM: half-metal, M: metal, I: insulator.

3D								2D			
Phase	Reference	Space Gr.	Magnetism	C	CN _{TM}	CN _O	$d_{\text{TM-O}}$ (Å)	Phase	CN _{TM}	CN _O	$d_{\text{TM-O}}$ (Å)
<i>wz</i> -ScO	—	$P6_3mc^a$	NM ^a	—	6	6	2.216 ^d	<i>h</i> -ScO	3	3	2.017
<i>wz</i> -TiO	—	$P6_3mc^a$	NM ^a	—	4	4	2.033	<i>h</i> -TiO	3	3	1.921
<i>wz</i> -VO	—	$P6_3mc^a$	FM ^a	—	4	4	1.968	<i>h</i> -VO	3	3	1.908
<i>wz</i> -CrO	—	$P6_3mc^a$	AFM1 ^a	—	4	4	1.958	<i>h</i> -CrO	3	3	1.879
<i>wz</i> -MnO	[4, 5, 8, 9]	$P6_3mc$	<i>wz</i> -AFM3	SC	4	4	2.029	<i>h</i> -MnO	3	3	1.936
<i>rs</i> -ScO	—	$Fm\bar{3}m^a$	NM ^a	—	6	6	2.239	<i>sq</i> -ScO	4	4	2.111
ϵ -TiO	[1, 2]	$P\bar{6}_2M$	NM	M	6, 3	6, 3 ^e	2.111, 1.976 ^e	<i>sq</i> -TiO	4	4	2.019
distorted <i>rs</i> -VO	[2]	$R\bar{3}M$	AFM	M	6	6	2.141	<i>sq</i> -VO	4	4	1.986
<i>rs</i> -CrO	[3]	$Fm\bar{3}m$	AFM1 ^a	M	6	6	2.154	<i>sq</i> -CrO	4	4	1.988
<i>rs</i> -MnO	[4, 5, 6, 7]	$Fm\bar{3}m^b$	AFM2 ^b	SC	6	6	2.222	<i>sq</i> -MnO	4	4	2.029
bixbyite Sc_2O_3	[10]	$Ia\bar{3}$	NM ^a	I	6	4	2.136	<i>h</i> - Sc_2O_3	3	2	1.920
corundum Ti_2O_3	[11, 12, 13, 14]	$R\bar{3}c$	AFM1	SC	6	4	2.051	<i>h</i> - Ti_2O_3	3	2	1.826
monoclinic V_2O_3	[15, 16]	$I2/a$	AFM	SC	6	4	2.011	<i>h</i> - V_2O_3	3	2	1.784
corundum Cr_2O_3	[11, 17, 18]	$R\bar{3}c$	AFM	SC	6	4	1.993	<i>h</i> - Cr_2O_3	3	2	1.772
bixbyite Mn_2O_3	[6, 7, 19]	$Ia\bar{3}$	AFM	M	6	4	2.063	<i>h</i> - Mn_2O_3	3	2	1.778
—	—	—	—	—	—	—	—	<i>sq</i> - ScO_2	4	2	2.004
anatase TiO_2	[20, 21]	$I4_1/amd$	NM	SC	6	3	1.976	<i>sq</i> - TiO_2	4	2	1.873
Mo VO_2	[22, 29, 30, 31]	$P2_1/c$	FM	M	6	3	1.936	<i>sq</i> - VO_2	4	2	1.824
rutile CrO_2	[23, 24]	$P4_2/mnm$	FM	HM	6	3	1.907	<i>sq</i> - CrO_2	4	2	1.790
rutile MnO_2	[7, 25]	$P4_2/mnm$	(NC) AFM ^c	SC	6	3	1.897	<i>sq</i> - MnO_2	4	2	1.777

^a The *wz*-ScO, *wz*-TiO, *wz*-VO, *wz*-CrO, and *rs*-ScO phases, and the magnetic orderings for the aforementioned phases, and for *rs*-CrO and bixbyite Sc_2O_3 , are not found in literature. We calculated the ground state magnetism for these structures. For *rs*-ScO and *rs*-CrO, we compared the energies of the 7 magnetic orderings for the *rs* structure as described in [5]: our calculations suggest that *rs*-ScO is non-magnetic; and although Ref. [3] mentions that bulk *rs*-CrO can be AFM or FM, our results show that the AFM1 configuration is more stable than the FM configuration, by 119 meV/atom. In our calculations for bixbyite Sc_2O_3 , the AFM1 and FM orderings states all relaxed to NM.

^b MnO is in the *rs* structure and is paramagnetic with $T > T_N = 118$ K; below the Néel temperature, MnO is AFM2 with a rhombohedrally distorted structure ($\alpha=90.62^\circ$) determined by neutron scattering [26]. In 2006, it was found by refined neutron scattering that the rhombohedral MnO is in fact monoclinic [27]. However, DFT calculations usually neglect this slight deviation [5].

^c For rutile MnO_2 , the spiral non-collinear (NC) AFM is the real magnetic ground state. We considered only the collinear (CL) AFM solution due to limited computational power. The moderate difference between the two magnetic states was given by [7]: $\Delta E(\text{NC-CL}) = -47$ meV/f.u.

^d The Sc-sublayer and O-sublayer relaxed to the same plane. Thus the structure can be regarded as *h*-ScO monolayers stacked in the ABAB order.

^e There are two configurations of coordination in ϵ -TiO. Thus there are two sets of coordination numbers and two different bond lengths.

References Table S2

- [1] Amano S, Bogdanovski D, Yamane H, Terauchi M and Dronskowski R, 2016, *Angew. Chem. Int. Ed.*, **55**, 1652.
- [2] Zhu L, Zhou J, Guo Z and Sun Z, 2016, *J. Phys. Chem. C*, **120**, 10009.
- [3] Rivadulla F, Fernández-Rossier J, García-Hernández M, López-Quintela M A, Rivas J and 5 J B G, 2007, *Phys. Rev. B*, **76**, 205110.
- [4] Nam K M, Kim Y I, Jo Y, Lee S M, Kim B G, Choi R, Choi S I, Song H and Park J T, 2012, *J. Am. Chem. Soc.*, **134**, 8392.
- [5] Schrön A, Rödl C and Bechstedt F, 2010, *Phys. Rev. B*, **82**, 165109.
- [6] Franchini C, Podloucky R, Paier J, Marsman M and Kresse G, 2007, *Phys. Rev. B*, **75**, 195128.
- [7] Lim J S, Saldana-Greco D and Rappe A M, 2016, *Phys. Rev. B*, **94**, 165151.
- [8] Gopal P, Spaldin N A and Waghmare U V, 2004, *Phys. Rev. B*, **70**, 205104.
- [9] Kan E, Li M, Hu S, Xiao C, Xiang H and Deng K, 2013, *J. Phys. Chem. Lett.*, **4**, 1120.
- [10] Jacobs R M, Booske J H and Morgan D, 2012, *Phys. Rev. B*, **86**, 054106.
- [11] Guo Y, Clark S J and Robertson J, 2014, *J. Chem. Phys.*, **140**, 054702.
- [12] Gerosa M, Bottani C E, Caramella L, Onida G, Valentin C D and Pacchioni G, 2015, *Phys. Rev. B*, **91**, 155201.
- [13] Hu Z and Metiu H, 2011, *J. Phys. Chem. C*, **115**, 5841.
- [14] Singh V and Pulikkotil J, 2016, *J. Alloys Compd.*, **658**, 430.
- [15] Grieger D and Fabrizio M, 2015, *Phys. Rev. B*, **92**, 075121.
- [16] Leonov I, Anisimov V I and Vollhardt D, 2015, *Phys. Rev. B*, **91**, 195115.
- [17] Shi S, Wysocki A L and Belashchenko K D, 2009, *Phys. Rev. B*, **79**, 104404.
- [18] Stashans A and Jácome S, 2014, *Comput. Mater. Sci.*, **81**, 353.
- [19] Cockayne E, Levin I, Wu H and Llobet A, 2013, *Phys. Rev. B*, **87**, 184413.
- [20] Luo Y, Benali A, Shulenburg L, Krogel J T and Kent O H P R C, 2016, *arXiv*, **1607**, 07361v2.
- [21] Peng H, Li J, Li S S and Xia J B, 2009, *Phys. Rev. B*, **79**, 092411.
- [22] Xu S, Shen X, Hallman K A, F R and Haglund J, 2016, *arXiv*, **1606**, 03162.
- [23] Schwarz K, 1986, *J. Phys. F: Met. Phys.*, **16**, L211.
- [24] Solovyev I V, Kashin I V and Mazurenko V V, 2015, *Phys. Rev. B*, **92**, 144407.
- [25] Kitchaev D A, Peng H, Liu Y, Sun J, Perdew J P and Ceder G, 2016, *Phys. Rev. B*, **93**, 045132.
- [26] Shaked H, J Faber J and Hitterman R L, 1988, *Phys. Rev. B*, **38**, 11901.
- [27] Goodwin A L, Tucker M G, Dove M T and Keen D A, 2006, *Phys. Rev. Lett.*, **96**, 047209.
- [28] Ataca C, S, ahin H and Ciraci S, 2012, *J. Phys. Chem. C*, **116**, 8983.
- [29] Xiao X, Song H, Lin S, Zhou Y, Zhan X, Hu Z, Zhang Q, Sun J, Yang B, Li T, Jiao L, Zhou J, Tang J and Gogotsi Y, 2015, *Nature Commun.*, **7**, 11296.
- [30] Zheng H and Wagner L K, 2015, *Phys. Rev. Lett.*, **114**, 176401.
- [31] Eyert V, 2011, *Phys. Rev. B*, **107**, 016401.

Table S3. (Average) bond lengths in Å at 0 K prior to AIMD simulation; and average, minimum, and maximum bond lengths in Å for the structures that showed no bond breaking during AIMD simulation, at 300 K and 700 K. That bond lengths can be evaluated does not necessarily imply that a structure is thermally stable: a number of structures for which bond lengths are listed in this Table, were found to restructure into energetically more favorable configurations, and as such are considered to be thermally unstable.

	0 K		300 K			700 K		
			avrg	min	max	avrg	min	max
<i>h</i> -ScO	2.017		2.039	1.831	2.361	2.050	1.773	2.657
<i>h</i> -TiO	1.921		1.959	1.751	2.297	1.970	1.626	2.674
<i>h</i> -VO	1.908		1.916	1.727	2.224	1.934	1.641	2.473
<i>h</i> -CrO	1.879		1.921	1.729	2.301	1.931	1.639	2.727
<i>h</i> -MnO	1.936		1.972	1.763	2.290	1.982	1.667	2.556
<i>sq</i> -ScO	2.111		2.138	1.916	2.440	2.153	1.816	2.877
<i>sq</i> -TiO	2.019		2.039	1.841	2.357	2.059	1.725	2.542
<i>sq</i> -VO	1.986		2.002	1.820	2.301	2.018	1.738	2.625
<i>sq</i> -CrO	1.988		2.007	1.801	2.263	2.019	1.744	2.544
<i>sq</i> -MnO	2.029		2.059	1.801	2.698	—	—	—
<i>h</i> -Sc ₂ O ₃	1.920		1.941	1.808	2.095	1.958	1.770	2.261
<i>h</i> -Ti ₂ O ₃	1.826		1.847	1.710	2.008	1.862	1.672	2.203
<i>h</i> -V ₂ O ₃	1.785		1.804	1.674	1.989	1.818	1.612	2.139
<i>h</i> -Cr ₂ O ₃	1.772		1.796	1.664	2.032	1.813	1.596	2.204
<i>h</i> -Mn ₂ O ₃	1.778		1.805	1.600	2.124	1.825	1.552	2.423
<i>sq</i> -ScO ₂	2.004		2.069	1.857	2.441	—	—	—
<i>sq</i> -TiO ₂	1.873		—	—	—	—	—	—
<i>sq</i> -VO ₂	1.824		—	—	—	—	—	—
<i>sq</i> -CrO ₂	1.790		—	—	—	—	—	—
<i>sq</i> -MnO ₂	1.777		—	—	—	—	—	—

Table S4. DFT (GGA-PBE) and HSE06 calculated electronic and magnetic properties of the 2D TMO phases. EGS: electronic ground state, MGS: magnetic ground state. TM: transition metal atom, O: oxygen atom. SC: semiconductor, SM: semimetal, HM: half-metal, M: metal. Band gaps are for spin-up (\uparrow) and spin-down (\downarrow) electrons. Magnetic moments were evaluated from spin-up and spin-down electron densities within Bader volumes.

Phase	Method	EGS	MGS	Band gap (eV)		Mag. moment (μ_B)		Bader charge (e)	
				\uparrow	\downarrow	TM	O	TM	O
<i>t</i> -VO	DFT	SC	AFM2	0.15	0.15	± 1.72	± 0.02	1.04	-1.04
	HSE	SC	AFM2	1.16	1.16	± 2.27	± 0.04	1.09	-1.09
<i>t</i> -CrO	DFT	SC	AFM2	0.40	0.40	± 2.93	± 0.03	1.11	-1.11
	HSE	SC	AFM2	0.60	0.60	± 3.36	± 0.06	1.09	-1.09
<i>t</i> -MnO	DFT	SC	AFM1	0.18	0.18	± 4.03	± 0.08	1.19	-1.19
	HSE	SC	AFM1	1.69	1.69	± 4.42	± 0.07	1.30	-1.30
<i>h</i> -ScO	DFT	SC	AFM	0.36	0.36	± 0.23	0.00	1.32	-1.32
	HSE	SC	AFM	1.05	1.05	± 0.21	± 0.02	1.41	-1.41
<i>h</i> -TiO	DFT	SC	NM	0.22	—	—	—	1.19	-1.19
	HSE	SC	NM	0.28	—	—	—	1.27	-1.27
<i>h</i> -VO	DFT	SC	FM	0.51	5.16	2.80	0.20	1.24	-1.24
	HSE	SC	FM	0.55	6.77	2.86	0.14	1.29	-1.29
<i>h</i> -CrO	DFT	SC	AFM	0.62	0.62	± 3.38	± 0.05	1.20	-1.20
	HSE	M	AFM	—	—	± 3.66	± 0.08	1.32	-1.32
<i>h</i> -MnO	DFT	SC	AFM	0.63	0.63	± 4.37	± 0.10	1.28	-1.28
	HSE	SC	AFM	2.11	2.11	± 4.61	± 0.08	1.42	-1.42
<i>sq</i> -ScO	DFT	M	NM	—	—	—	—	1.51	-1.51
	HSE	M	NM	—	—	—	—	1.62	-1.62
<i>sq</i> -TiO	DFT	M	AFM1	—	—	± 1.03	0.00	1.39	-1.39
	HSE	M	AFM1	—	—	± 1.22	0.00	1.50	-1.50
<i>sq</i> -VO	DFT	SC	AFM1	0.36	0.36	± 3.46	0.00	1.40	-1.40
	HSE	SC	AFM1	3.12	3.12	± 3.66	0.00	1.46	-1.46
<i>sq</i> -CrO	DFT	M	AFM1	—	—	± 2.33	0.00	1.36	-1.36
	HSE	M	AFM1	—	—	± 2.61	0.00	1.45	-1.45
<i>sq</i> -MnO	DFT	M	AFM1	—	—	± 4.20	0.00	1.31	-1.31
	HSE	SM	AFM1	-0.04	-0.04	± 4.64	0.00	1.44	-1.44
<i>h</i> -Sc ₂ O ₃	DFT	SC	NM	2.89	—	—	—	1.88	-1.25
	HSE	SC	NM	4.35	—	—	—	1.99	-1.33
<i>h</i> -Ti ₂ O ₃	DFT	SC	AFM	0.93	0.93	± 0.87	0.00	1.69	-1.13
	HSE	SC	AFM	3.23	3.23	± 0.95	0.00	1.81	-1.21
<i>h</i> -V ₂ O ₃	DFT	HM	FM	—	4.32	2.00	0.00	1.56	-1.04
	HSE	HM	FM	—	6.24	2.10	-0.06	1.65	-1.10
<i>h</i> -Cr ₂ O ₃	DFT	HM	FM	—	3.94	2.96	0.02	1.51	-1.01
	HSE	SC	FM	0.88	5.73	2.93	0.05	1.65	-1.10
<i>h</i> -Mn ₂ O ₃	DFT	SC	FiM	0.62	0.93	4.15; -2.24	0.03	1.45	-0.97
	HSE	SC	FiM	3.02	3.77	4.55; -2.69	0.05	1.44	-1.02

Table S4 continued. DFT (GGA-PBE) and HSE06 calculated electronic and magnetic properties of the 2D TMO phases. EGS: electronic ground state, MGS: magnetic ground state. TM: transition metal atom, O: oxygen atom. SC: semiconductor, SM: semimetal, HM: half-metal, M: metal. Band gaps are for spin-up (\uparrow) and spin-down (\downarrow) electrons. Magnetic moments were evaluated from spin-up and spin-down electron densities within Bader volumes.

Phase	Method	EGS	MGS	Band gap (eV)		Mag. moment (μ_B)		Bader charge (e)	
				\uparrow	\downarrow	TM	O	TM	O
<i>sq</i> -ScO ₂	DFT	HM	FM	3.26	—	−0.05	0.53	1.98	−0.99
	HSE	HM	FM	5.21	—	−0.09	0.54	2.08	−1.04
<i>sq</i> -TiO ₂	DFT	SM	NM	−0.002	—	—	—	2.09	−1.04
	HSE	SC	NM	0.13	—	—	—	2.28	−1.14
<i>sq</i> -VO ₂	DFT	HM	FM	−0.36 ^a	0.81	0.18	−0.09	1.86	−0.93
	HSE	SC	FM	0.65	1.93	1.12	−0.06	2.06	−1.03
<i>sq</i> -CrO ₂	DFT	HM	FM	—	0.46	2.22	−0.11	1.75	−0.88
	HSE	HM	FM	—	2.91	2.54	−0.27	1.93	−0.97
<i>sq</i> -MnO ₂	DFT	M	AFM1	—	—	±2.58	0.03	1.68	−0.84
	HSE	HM	AFM1	4.07	—	±3.48	0.50	1.93	−0.96

^a Semimetal.

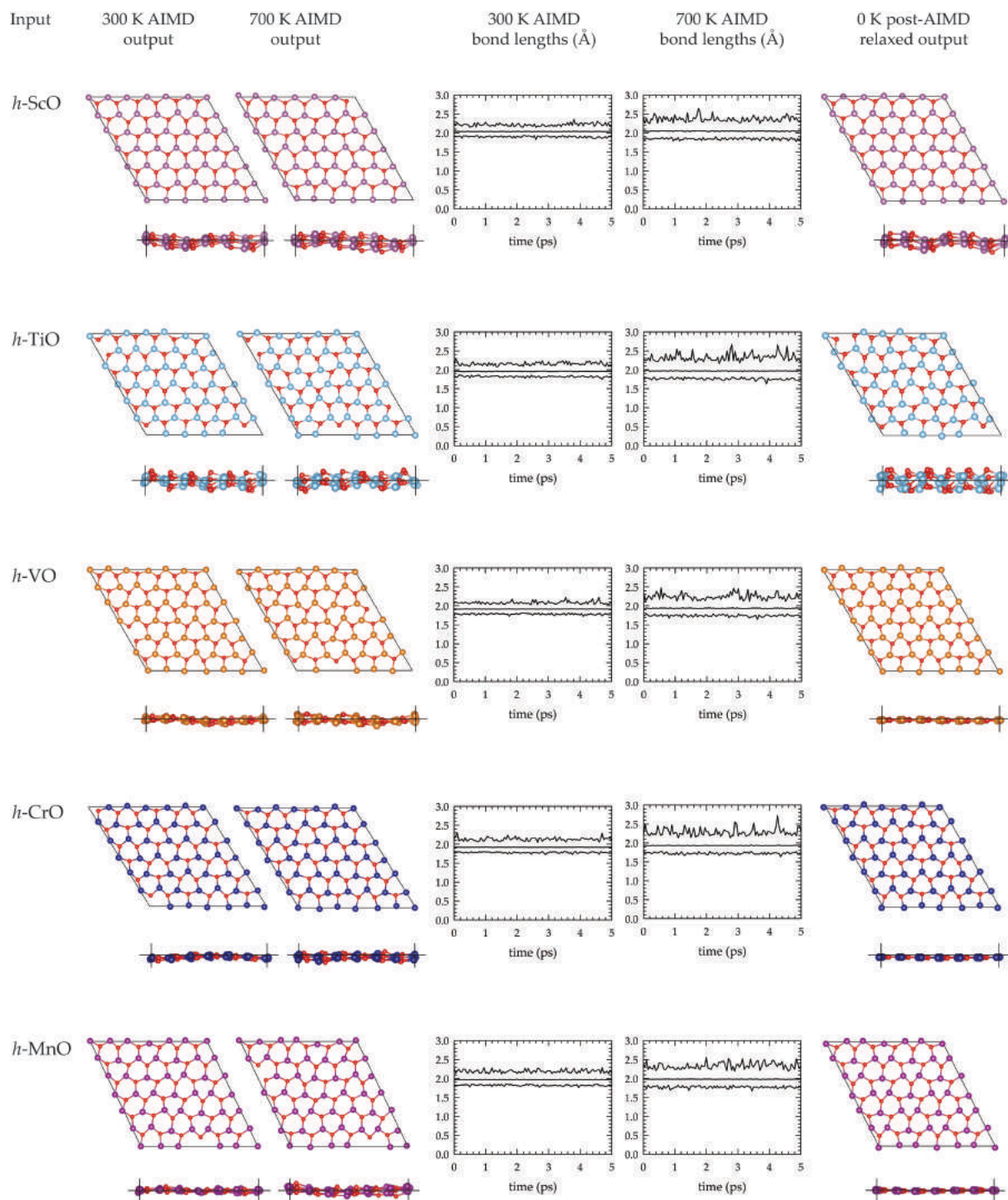


Figure S1. AIMD output configurations as obtained after 2 ps equilibration and 5 ps canonical (NVT) ensemble simulation at 300 K and 700 K; minimum, average, and maximum bond lengths, for the structures that showed no bond breaking during the 5 ps NVT simulation; and post-AIMD relaxation output configurations as obtained after 0 K relaxation of the 300 K AIMD output configurations.

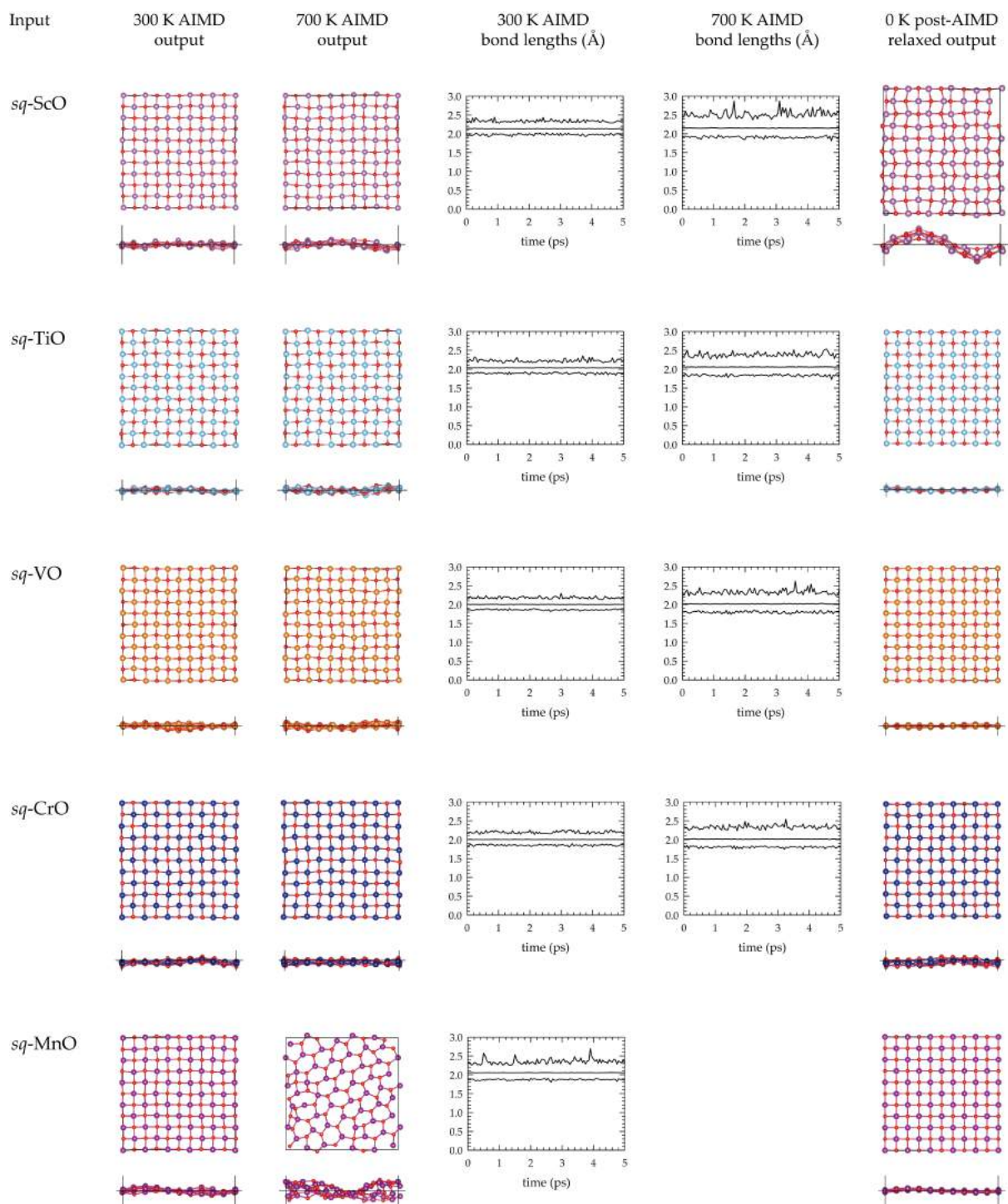


Figure S1 continued. AIMD output configurations as obtained after 2 ps equilibration and 5 ps canonical (NVT) ensemble simulation at 300 K and 700 K; minimum, average, and maximum bond lengths, for the structures that showed no bond breaking during the 5 ps NVT simulation; and post-AIMD relaxation output configurations as obtained after 0 K relaxation of the 300 K AIMD output configurations.

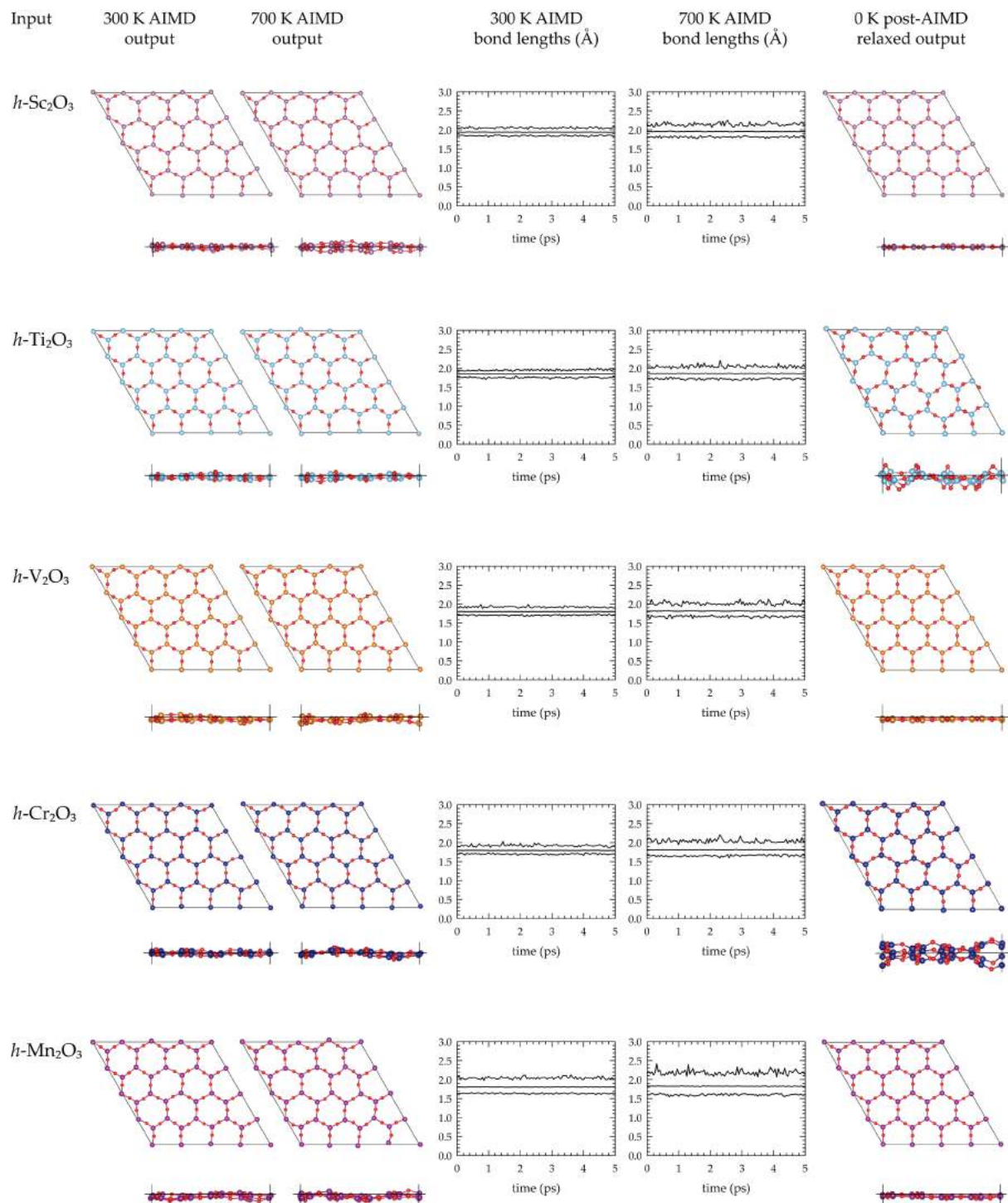


Figure S1 continued. AIMD output configurations as obtained after 2 ps equilibration and 5 ps canonical (NVT) ensemble simulation at 300 K and 700 K; minimum, average, and maximum bond lengths, for the structures that showed no bond breaking during the 5 ps NVT simulation; and post-AIMD relaxation output configurations as obtained after 0 K relaxation of the 300 K AIMD output configurations.

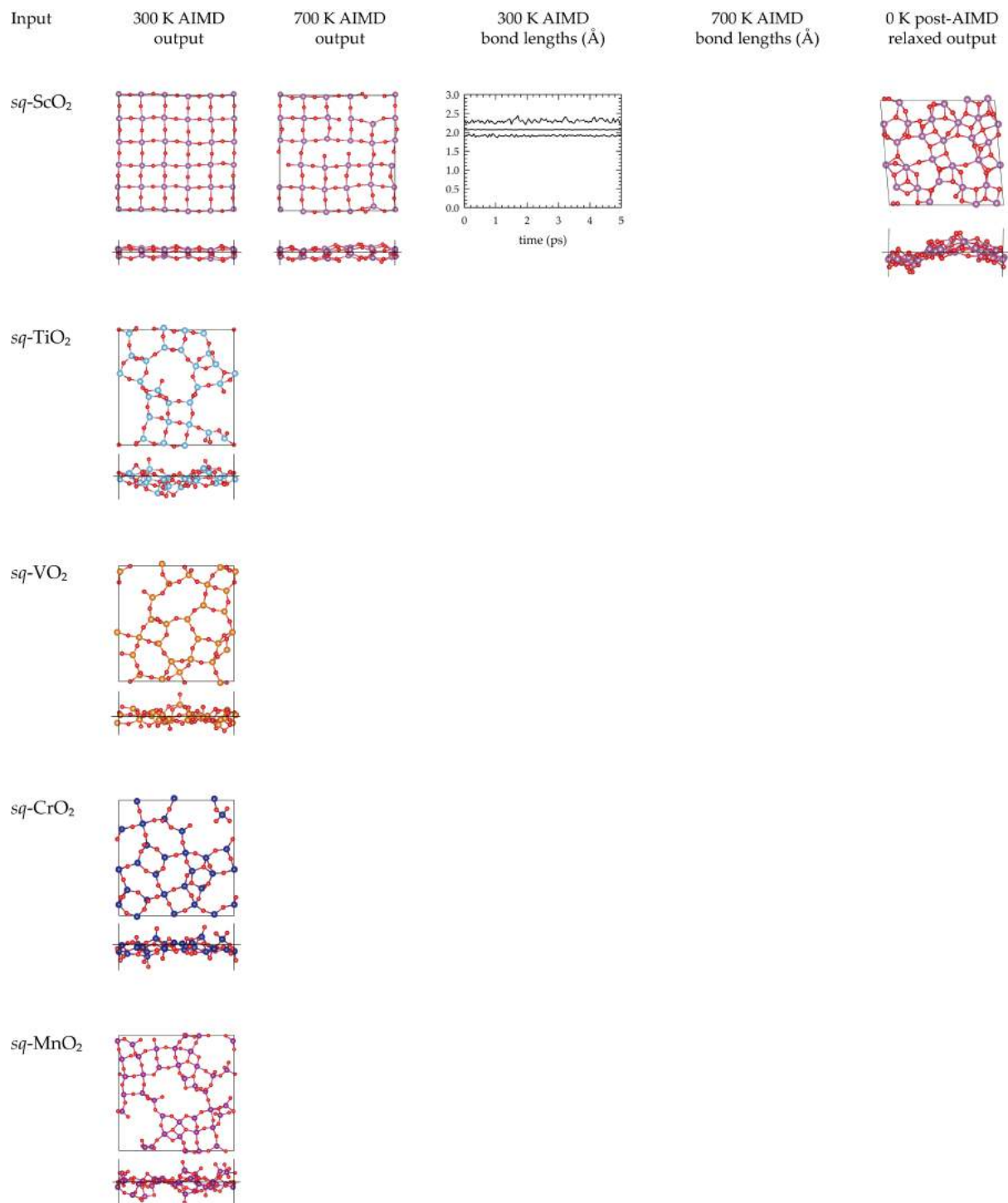
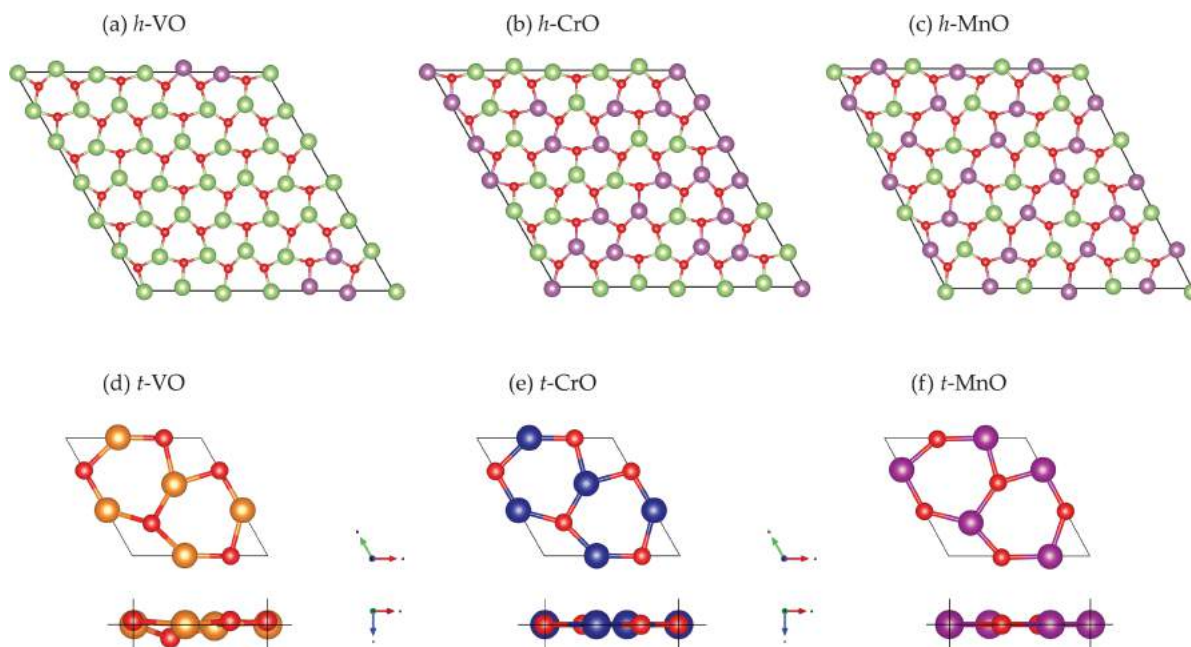


Figure S1 continued. AIMD output configurations as obtained after 2 ps equilibration and 5 ps canonical (NVT) ensemble simulation at 300 K and 700 K; minimum, average, and maximum bond lengths, for the structures that showed no bond breaking during the 5 ps NVT simulation; and post-AIMD relaxation output configurations as obtained after 0 K relaxation of the 300 K AIMD output configurations.



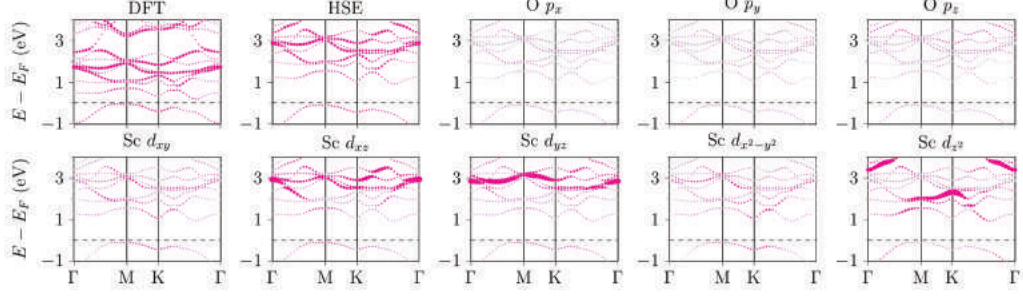
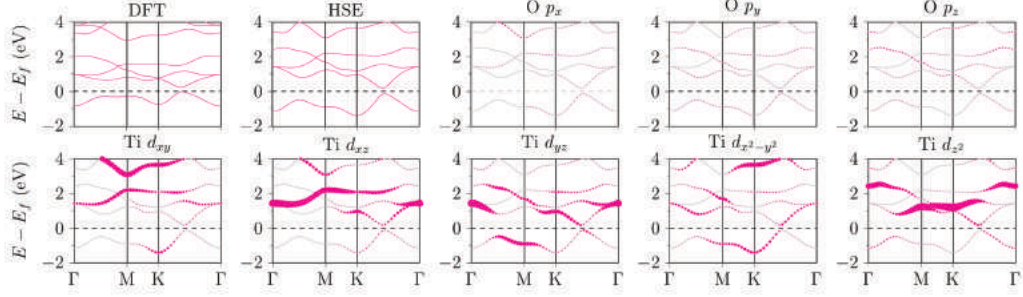
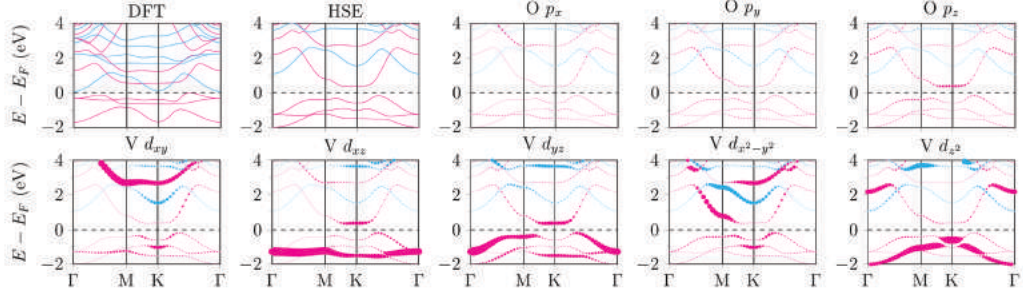
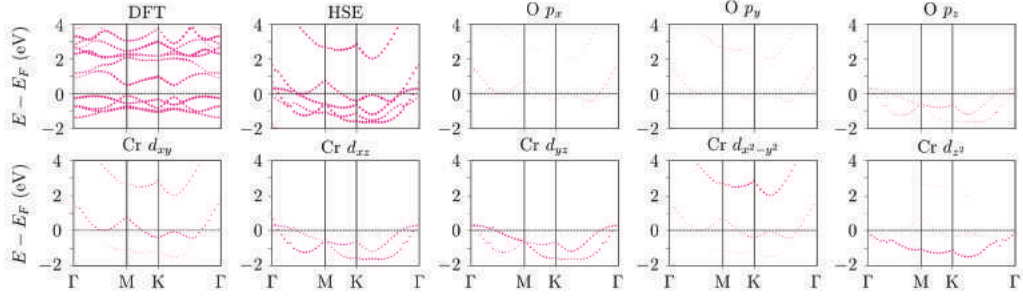
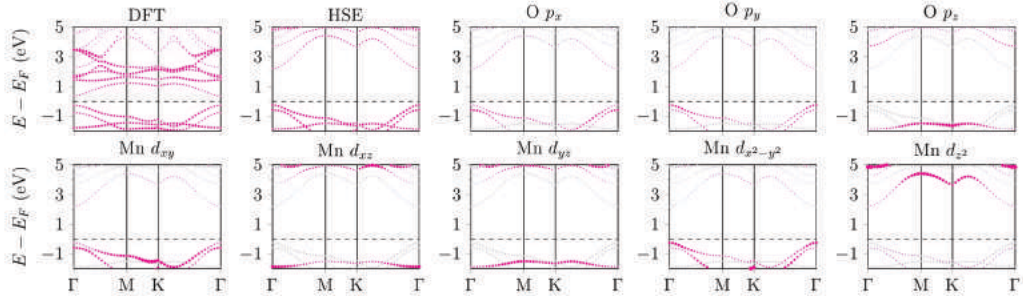
(a) *h*-ScO AFM(b) *h*-TiO NM(c) *h*-VO FM(d) *h*-CrO AFM(e) *h*-MnO AFM

Figure S3. DFT and HSE band structures, and HSE orbital-resolved band structures, of the magnetic ground state of the *h*-MO phases. For spin-polarized configurations, spin-down bands are shown in cyan when spin-up and spin-down bands do not overlap.

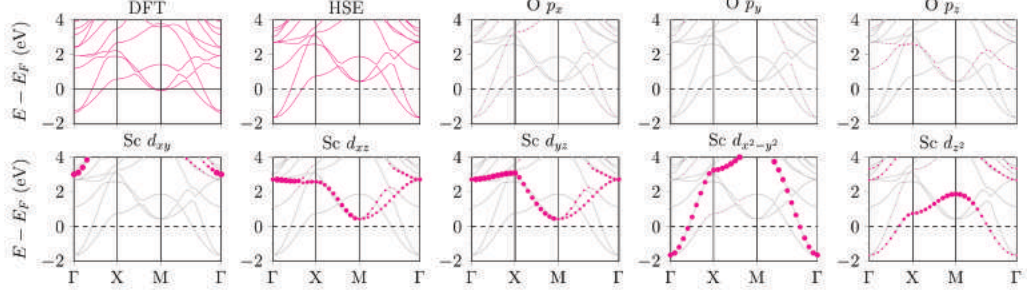
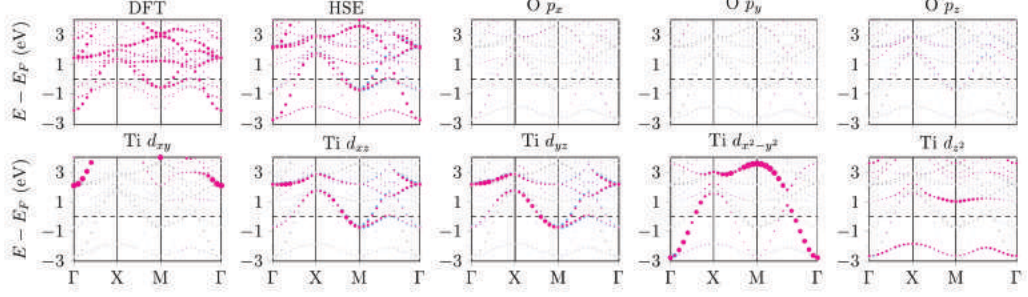
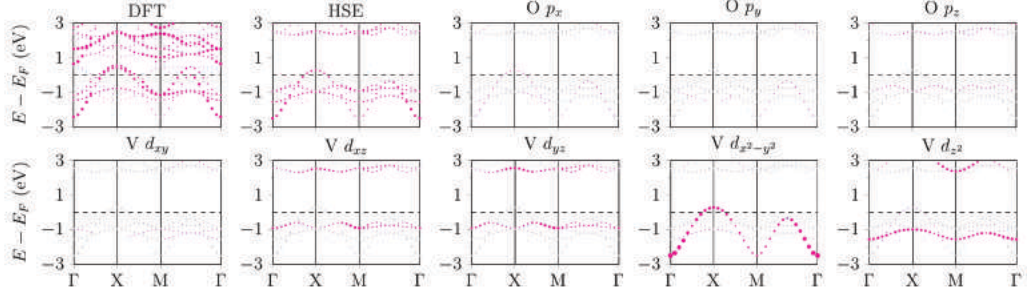
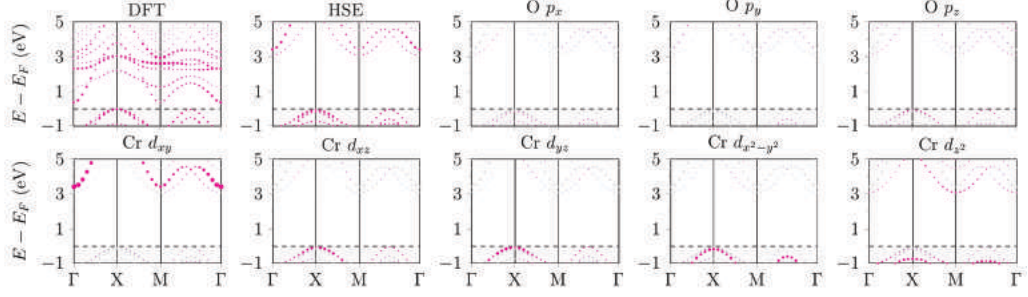
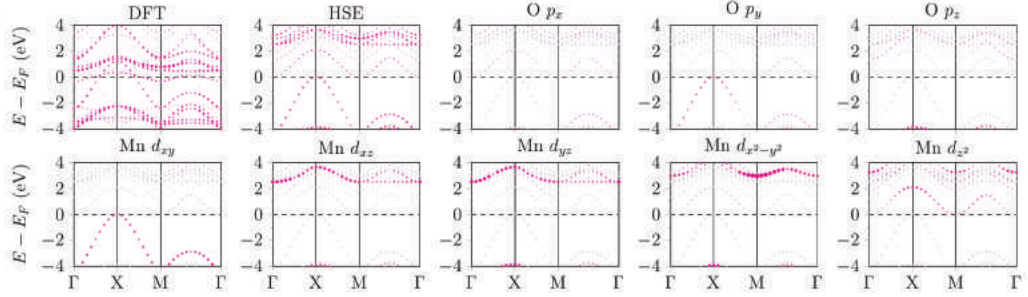
(f) *sq*-ScO NM(g) *sq*-TiO AFM1(h) *sq*-VO AFM1(i) *sq*-CrO AFM1(j) *sq*-MnO AFM1

Figure S3 continued. DFT and HSE band structures, and HSE orbital-resolved band structures, of the magnetic ground state of the *sq*-MO phases. For spin-polarized configurations, spin-down bands are shown in cyan when spin-up and spin-down bands do not overlap.

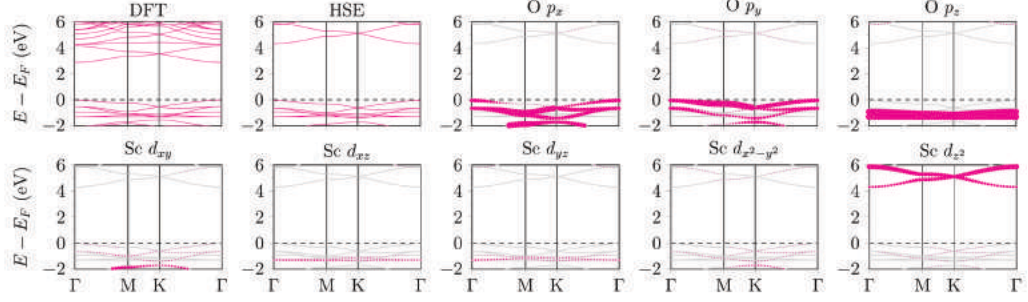
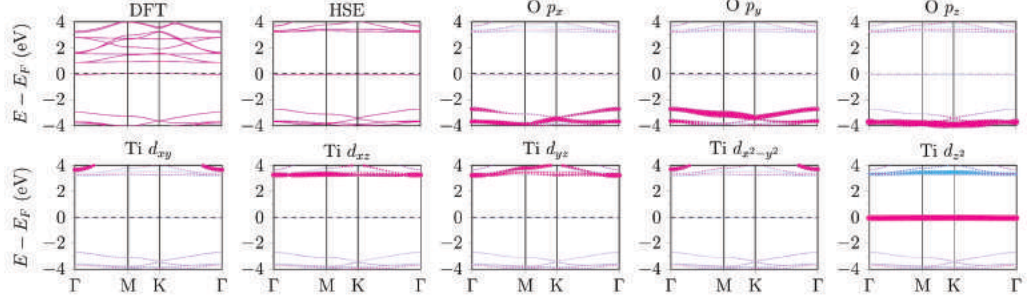
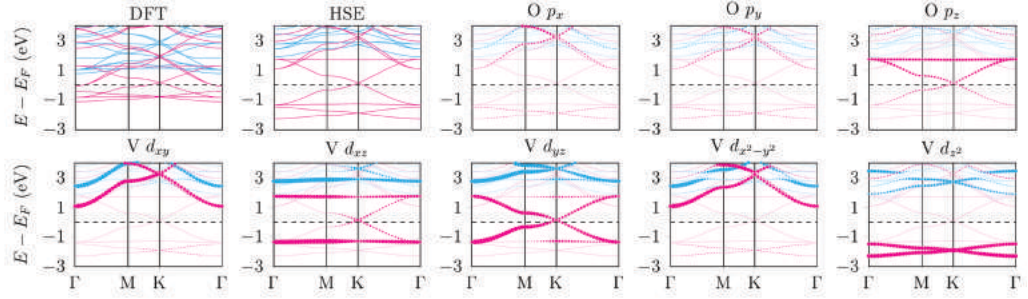
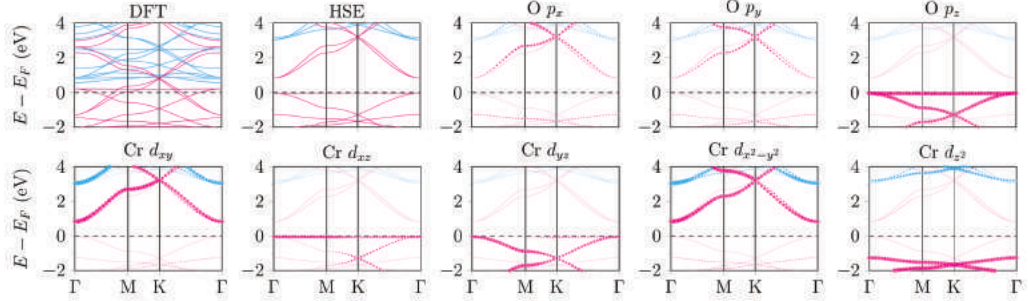
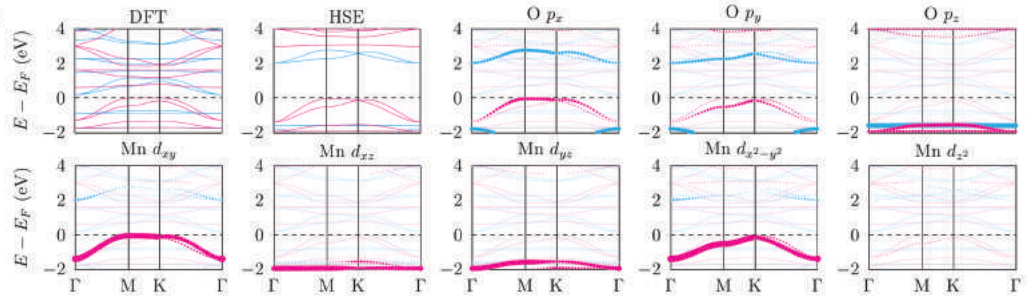
(k) h -Sc₂O₃ NM(l) h -Ti₂O₃ AFM(m) h -V₂O₃ FM(n) h -Cr₂O₃ FM(o) h -Mn₂O₃ AFM

Figure S3 continued. DFT and HSE band structures, and HSE orbital-resolved band structures, of the magnetic ground state of the h -M₂O₃ phases. For spin-polarized configurations, spin-down bands are shown in cyan when spin-up and spin-down bands do not overlap.

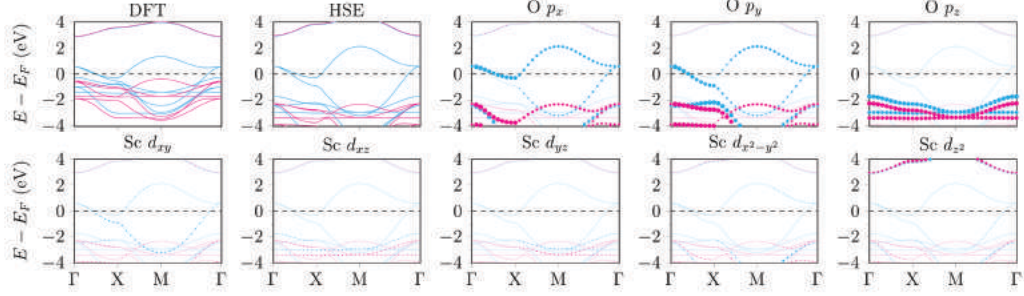
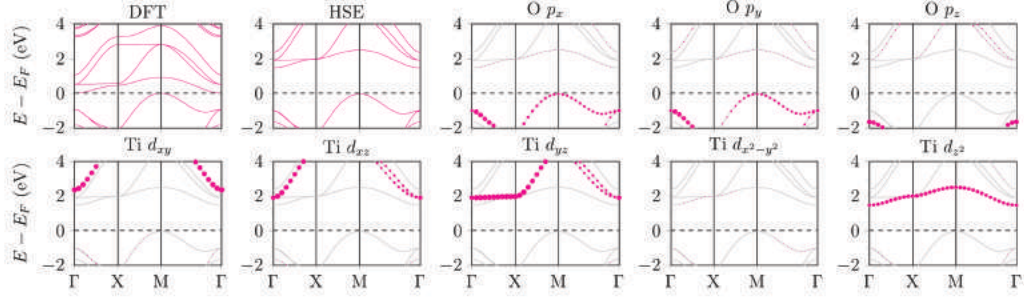
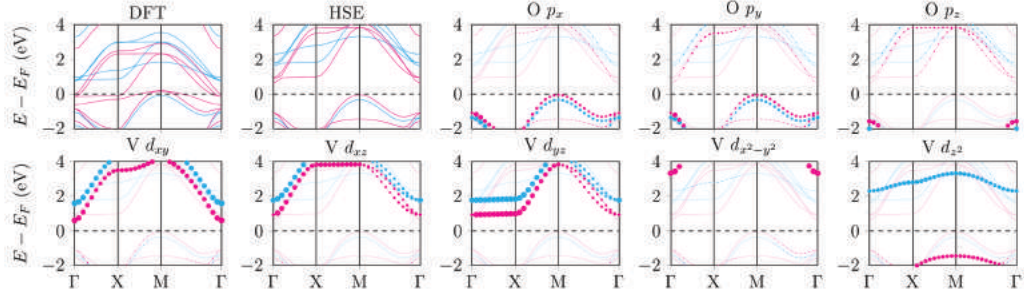
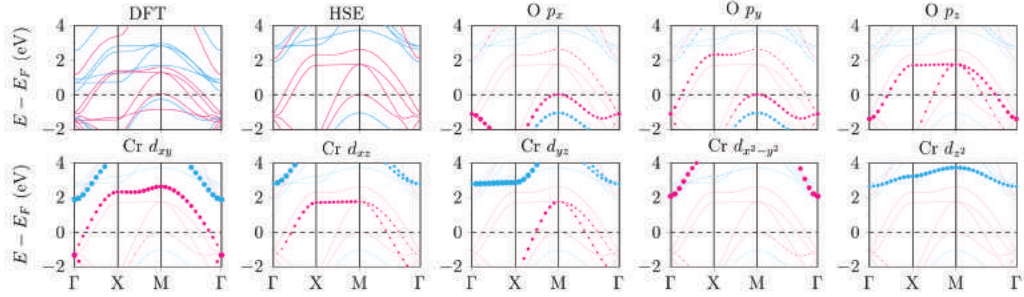
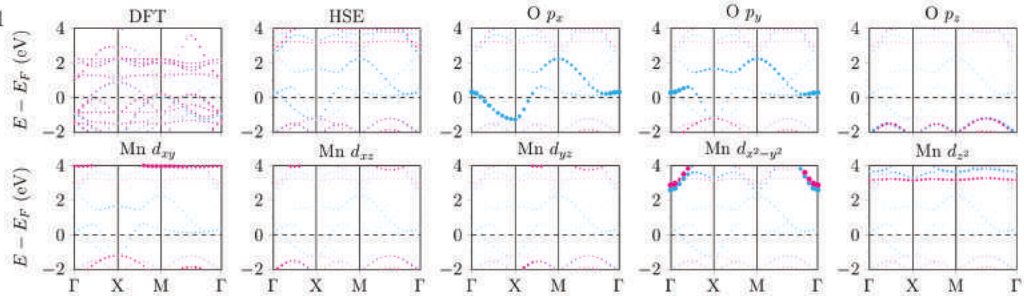
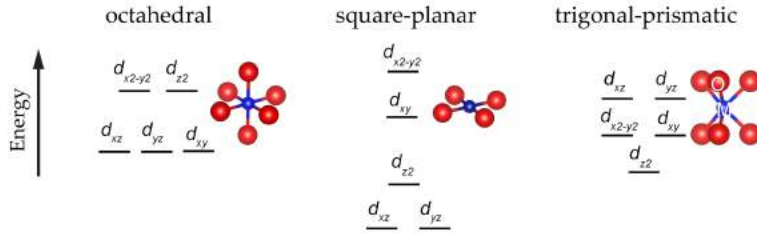
(p) *sq*-ScO₂ FM(q) *sq*-TiO₂ NM(r) *sq*-VO₂ FM(s) *sq*-CrO₂ FM(t) *sq*-MnO₂ AFM1

Figure S3 continued. DFT and HSE band structures, and HSE orbital-resolved band structures, of the magnetic ground state of the *sq*-MO₂ phases. For spin-polarized configurations, spin-down bands are shown in cyan when spin-up and spin-down bands do not overlap.

(a) crystal field splitting pattern



(b) projected density of states

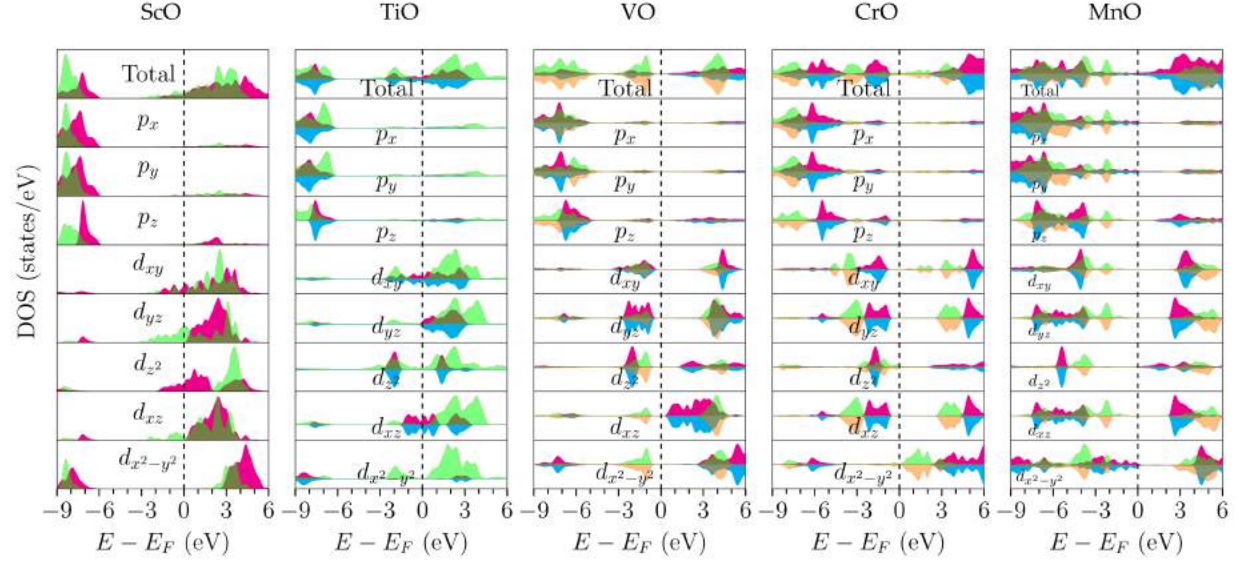


Figure S4. Top panel, (a): TM atom coordination and TM d orbital splitting pattern in the 2D square-planar and 3D octahedral and 3D trigonal-prismatic crystal fields. Bottom panel, (b): Projected density of states of O p and TM d orbitals for the 2D sq -MO and their corresponding 3D bulk MO phases. The Fermi energy is set to zero and indicated with a dashed line. Pink and blue indicate spin-up and spin-down states of the 2D phases; orange and green indicate spin-up and spin-down states of the 3D phases. Please note that for visualization effects and to allow easier comparison by the reader, the DOS plots in this Figure were generated with a wider Gaussian smearing than actually used for the total-energy and band structure calculations.

Supplementary Discussion

Energetic Stability of 2D *sq*-MOs over 3D Counterparts. To further understand the underlying reason for the energetic stability of the thermally stable *sq*-TiO and *sq*-MnO phases over their corresponding bulk phases (see the section on the energetic stability of 2D TMO phases with respect to bulk), we compared the orbital-resolved density-of-states (DOS) for these two 2D TMOs to the DOS of their 3D counterparts.

It is informative to briefly review the crystal field splitting of the 2D *sq*-TMO systems and their corresponding 3D TMO systems (see Figure S4). In the bulk *rs*-TMO systems, each TM atom is surrounded by six oxygen atoms in an octahedral coordination. Under the octahedral crystal field, the five formerly degenerate *d* orbitals of this TM atom split into two groups of orbitals, where the d_{xz} , d_{yz} , and d_{xy} orbitals will have a lower energy than the d_{z^2} and $d_{x^2-y^2}$ orbitals, which will be higher in energy. This crystal field splitting pattern can be seen in the DOS for *rs*-MnO (and for *rs*-ScO, distorted *rs*-VO, and *rs*-CrO as well) in Figure S4. In bulk ϵ -TiO, each TM atom is surrounded by six oxygen atoms in a trigonal-prismatic coordination. As such, the *d* orbitals of the TM atoms split into three groups of orbitals, consisting of, with increasing energy: (1) d_{z^2} ; (2) $d_{x^2-y^2}$ and d_{xy} ; and (3) d_{xz} and d_{yz} orbitals. This pattern too can be seen in Figure S4, in terms of the *d*-band splitting in the DOS of ϵ -TiO.

For the 2D *sq*-MOs, the removal of two oxygen nearest neighbors results in the lowering of the crystal field symmetry from 3D octahedral or 3D trigonal-prismatic to 2D square-planar. As a consequence, under the square-planar crystal field, the *d* orbitals are further split: Compared to the octahedral crystal field, under the square-planar crystal field, the *d* orbitals with a *z* component will be lowered in energy as their overlap with the oxygen *p* orbitals is reduced; the degeneracy of the d_{z^2} and the $d_{x^2-y^2}$ orbitals will be broken, and the d_{z^2} orbital will have a lower energy; likewise, the d_{xz} and d_{yz} orbitals will be lowered in energy away from the d_{xy} orbital. The square-planar crystal field breaks the degeneracy of the $d_{x^2-y^2}$ and the d_{xy} orbitals in the trigonal-prismatic field in a similar way. The final pattern of splitting of the *d* orbitals under a square-planar crystal field is thus given as follows, in order of increasing energy: (1) d_{xz} and d_{yz} ; (2) d_{z^2} ; (3) d_{xy} ; and (4) $d_{x^2-y^2}$. For MnO and TiO, this loss of degeneracy and shifting in energy of orbitals can be observed in their DOS (see Figure S4). Note, for example, how in MnO the *d* orbitals split according to the square-planar crystal field splitting pattern, and how the d_{z^2} orbital, and the degenerate d_{xz} and d_{yz} orbitals, clearly shift to lower energies in the 2D system. This shifting to lower energies can also be observed for TiO. The other *sq*-MOs do not seem to follow this trend (see Figure S4). Based on this discussion of crystal field theory and the DOS, we think that the possible reason for the energetic stability of 2D *sq*-TiO and 2D *sq*-MnO over their 3D counterparts may be attributed to the fact that in these two systems, the splitting of the *d* orbitals under the square-planar crystal field stabilizes the system more than the *d* orbital splitting in the trigonal-prismatic and octahedral crystal fields does.

Supplementary Video

Supplementary Video 1 shows the transformation of 2D *sq*-MnO to 2D *t*-MnO during a 2 ps AIMD equilibration at 700 K.